Selective-area chemical beam epitaxy of in-plane InAs one-dimensional channels grown on InP(001), InP(111)B, and InP(011) surfaces

Lee, Joon Sue; Koelling, Sebastian; Verheijen, Marcel A.; Petkovic, Ivana; Schaller, Vanessa; Marcus, Charles M.; Krogstrup, Peter; Kouwenhoven, Leo P.; Bakkers, Erik P.A.M.; More Authors

DOI
10.1103/PhysRevMaterials.3.084606

Publication date
2019

Document Version
Final published version

Published in
Physical Review Materials

Editors' Suggestion

Selective-area chemical beam epitaxy of in-plane InAs one-dimensional channels grown on InP(001), InP(111)B, and InP(011) surfaces

Joon Sue Lee,[1] Sukgeun Choi,[2] Mihir Pendharkar,[2] Daniel J. Pennachio,[3] Brian Markman,[2] Michael Seas,[3] Sebastian Koelling,[4] Marcel A. Verheijen,[4] Lucas Casparis,[5,6] Karl D. Petersson,[5,6] Ivana Petkovic,[5,6] Vanessa Schaller,[7] Mark J. W. Rodwell,[2] Charles M. Marcus,[5,6] Peter Krogstrup,[5,8] Leo P. Kouwenhoven,[9] Erik P. A. M. Bakkers,[4] and Chris J. Palmstrøm[1,2,3,*]

[1]*California NanoSystems Institute, University of California, Santa Barbara, California 93106, USA*
[2]*Electrical and Computer Engineering Department, University of California, Santa Barbara, California 93106, USA*
[3]*Materials Department, University of California, Santa Barbara, California 93106, USA*
[4]*Department of Applied Physics, Eindhoven University of Technology, 5600 MB Eindhoven, The Netherlands*
[5]*Center for Quantum Devices, Niels Bohr Institute, University of Copenhagen, Universitetsparken 5, 2100 Copenhagen, Denmark*
[6]*Microsoft Quantum - Copenhagen, University of Copenhagen, Universitetsparken 5, 2100 Copenhagen, Denmark*
[7]*QuTech, Delft University of Technology, Delft, 2600 GA, The Netherlands*
[8]*Microsoft Quantum Materials Lab Copenhagen, Kanalvej 7, 2800 Kongens Lyngby, Denmark*
[9]*Microsoft Station Q Delft, Delft, 2600 GA, The Netherlands*

(Received 17 March 2019; published 26 August 2019)

We report on the selective-area chemical beam epitaxial growth of InAs in-plane, one-dimensional (1D) channels using patterned SiO_2-coated InP(001), InP(111)B, and InP(011) substrates to establish a scalable platform for topological superconductor networks. Top-view scanning electron micrographs show excellent surface selectivity and dependence of major facet planes on the substrate orientations and ridge directions, and the ratios of the surface energies of the major facet planes were estimated. Detailed structural properties and defects in the InAs nanowires (NWs) were characterized by transmission electron microscopic analysis of cross-sections perpendicular to the NW ridge direction and along the NW ridge direction. Electrical transport properties of the InAs NWs were investigated using Hall bars, a field effect mobility device, a quantum dot, and an Aharonov-Bohm loop device, which reflect the strong spin-orbit interaction and phase-coherent transport characteristic present in the selectively grown InAs systems. This study demonstrates that selective-area chemical beam epitaxy is a scalable approach to realize semiconductor 1D channel networks with the excellent surface selectivity and this material system is suitable for quantum transport studies.

DOI: 10.1103/PhysRevMaterials.3.084606

I. INTRODUCTION

There is an increasing interest in one-dimensional (1D) III-V semiconductor nanowires (NWs) proximitized by superconductors that can potentially be used to realize topological superconducting phases [1,2]. Among III-V semiconductors, InAs and InSb have been of particular interest since InAs and InSb possess strong spin-orbit coupling and large g factors. Indeed, signatures of Majorana zero modes have been experimentally observed from superconductor-paired InAs and InSb NWs prepared by vapor-liquid-solid (VLS) epitaxy method [3–6].

Recently, as a method of realizing the in-plane 1D channels, selective-area epitaxy (SAE) has been used and growths of In(Ga)As and InSb lateral NW networks have been demonstrated by molecular beam epitaxy (MBE) and metal-organic chemical vapor phase epitaxy [7–13]. Since the network patterning and NW synthesis can be batch processed, this approach can be considered scalable. A superconducting layer such as Al can also be deposited *in vacuo* on the clean sidewall of NWs in a controllable manner. While the design and manipulation of NW networks are limited in the VLS method, SAE offers greater flexibility.

Chemical beam epitaxy (CBE) is known to be a highly suitable growth technique for SAE of semiconductors on dielectric-patterned substrates [14]. Use of metal-organic group-III precursor molecules in CBE renders an excellent surface selectivity in comparison to conventional solid-source MBE that has a significantly narrower growth window to achieve both good surface selectivity and good film morphology. Selectivity arises from the need for a sufficiently high surface diffusion of the group-III element on the dielectric mask to eliminate unwanted nucleation on the mask. For the SAE by CBE, the metal organic group-III precursor does not crack on the dielectric surface and only cracks on the semiconductor surface [15]. Hence, the growth window of CBE is larger than that of MBE with the lower bound and upper bound of the growth temperature being determined by the cracking temperatures of metal-organic precursor molecules on the semiconductor surface and by the decomposing temperatures of the grown semiconductor, respectively. As a result, selective-area CBE has been used to monolithically integrate InP-based optoelectronic devices [14].

*Author to whom correspondence should be addressed: cjpalm@ucsb.edu

Here, we apply CBE to selectively grow in-plane InAs NWs on InP(001), InP(111)B, and InP(011) surfaces pre-patterned with SiO_2 layers. The dependence of the InAs morphology on the V/III ratio was first examined. Then, the optimum In-rich growth conditions were applied for SAE InAs NWs, exhibiting excellent surface selectivity. For the desired topological superconductivity studies, NWs with fewer defects and higher carrier mobility are required. We characterized structural and electrical properties of the InAs NWs as a function of substrate orientations and ridge directions. Furthermore, field effect mobility, spin-orbit interaction, electron g factor, and phase-coherent transport were investigated in the InAs NWs grown on InP(001) substrates.

II. EXPERIMENTAL

All the substrates used for SAE in this work are lithographically patterned, SiO_2-coated, Fe-doped semi-insulating InP(001), InP(111)B, and InP(011) wafers. A 3-nm-thick Al_2O_3 etch-stop layer was first deposited by atomic layer deposition on the bare wafers, followed by plasma-enhanced chemical vapor deposition of a 30-nm-thick SiO_2 masking layer. The patterns were defined by electron-beam lithography and formed by inductively coupled plasma etching with a $CHF_3/CF_4/O_2$ gas mixture. The Al_2O_3 etch-stop layer was finally etched by tetramethyl-ammonium hydroxide (TMAH–$N(CH_3)_4OH$). The InP surface was further cleaned by a sequence of ultraviolet-ozone cleaning for 900 seconds, diluted HCl ($HCl : H_2O = 1:10$) etching for 60 seconds, and a final deionized H_2O rinse for 30 seconds. (The fabrication procedures are schematically shown in Ref. [16].)

SAE was carried out in a VG-Semicon V80H CBE system. Trimethylindium (TMI–$In[CH_3]_3$) and thermally cracked arsine (AsH_3) and phosphine (PH_3) were used as source materials. A gas injector cell kept at 75 °C was used for TMI and a modified low-pressure group-V hydride cracker cell kept at 1070 °C was used for AsH_3 and PH_3. The growth chamber base pressure was $\leqslant 1 \times 10^{-10}$ mbar but increased as high as $\sim 2 \times 10^{-5}$ mbar during growth due to the large amount of H_2 created from the thermal decomposition of AsH_3 and PH_3 gases.

A piece ($\sim 7 \times 7\,mm^2$) of reference InP(001) wafer was indium bonded onto the center of each 3-inch molybdenum sample holder for *in situ* growth monitoring. Optical pyrometry and reflection high-energy electron diffraction (RHEED) were employed to measure the substrate temperature and characterize the surface during growth, respectively. The patterned substrates were cleaved into $\sim 5 \times 5\,mm^2$-size square shapes, which were then co-mounted around the reference wafer on the same sample holder also using indium bonding. In the VG-Semicon CBE system, the V/III ratios were controlled by regulating the pressure of the group-III and group-V precursor gas supply lines [17]. In general, the group-V line pressure was kept constant while varying the group-III line pressure.

Prior to growth, the native oxide was thermally desorbed from the substrate surface in a P_2 environment at ~520 °C where the streaky (2 × 4) RHEED pattern is observed from the InP(001) reference sample. SAE was initiated by supplying TMI and growing a 9-nm-thick InP buffer layer. The line pressures for TMI and PH_3 were set to 0.5 and 25 Torr, respectively. The resulting growth rate was ~0.5 monolayer (ML)/sec. Then, the TMI valve was closed and growth was interrupted with PH_3 for 30 seconds to smoothen the InP surface. InAs growth started by closing the PH_3 valve and opening the TMI and AsH_3 valves simultaneously. While the growth temperature was kept at 515–520 °C, the V/III ratio was varied as a control parameter. To control the V/III ratio, the AsH_3 gas-line pressure was typically kept at 10 Torr and the TMI gas-line pressure varied. The TMI pressure was set to 0.3 Torr (~0.15 ML/sec) and 0.6 Torr (~0.60 ML/sec) for As-rich and In-rich growth, respectively. The transition from As-stabilized InAs(001) (2 × 4) RHEED patterns to In-stabilized InAs(001) (4 × 2) RHEED patterns was observed when the TMI pressure was at around 0.5 Torr.

For transport studies of topological superconductivity, it is crucial to have an electrically transparent interface between a semiconductor and a superconductor as evidenced in epitaxial Al-InSb NW devices which demonstrated the theoretically predicted quantized conductance [18,19]. We prepared the epitaxial Al in a separate ultrahigh-vacuum chamber interconnected to the CBE chamber. We note that growth of the Al layer by CBE is not viable because low temperature (lower than room temperature) is required for smooth Al morphology whereas the Al growth has been carried out in the same chamber for MBE SAE InAs NWs [9]. After the selective-area chemical beam epitaxy of the InAs NWs, we transferred the 3-inch molybdenum sample holder *in vacuo*. The epitaxial Al was grown by MBE at a growth rate of 0.16 nm/minute with the sample holder cooled down to ~80 K by liquid nitrogen on a cold-head manipulator. A clean interface between the Al and InAs was observed in an InAs NW along [100] direction grown on an InP(001) substrate. Low-temperature transport measurements of tunneling spectroscopy of normal-superconductor junctions show a hard superconducting gap, but the superconductivity study is beyond the scope of this paper.

The morphology of InAs NWs, crystallographic orientation of major facets, and surface selectivity were examined by a FEI Nova Nano 650 FEG SEM. High-angle annular dark field scanning transmission electron microscopy (HAADF-STEM) using a probe-corrected JEOL ARM200F and a FEI Titan 300 kV TEM/STEM system was used for cross-sectional analysis of the NWs. The cross-sectional specimens were prepared using focused Ga ion beam (FIB) etching. Before FIB etching, a thin carbon layer was thermally evaporated on the surface of NWs followed by deposition of a 2.5-μm-thick Pt protection layer in the FIB. FIB etching steps down to 2 kV were utilized to minimize possible damage to the lamella. The TEM lamellas were moved directly to an oxygen plasma cleaner before it was loaded into TEM/STEM systems to minimize contamination.

Electrical transport properties of the InAs NWs were characterized by Hall measurements at 2 K using a Quantum Design Physical Property Measurement System (PPMS) with magnetic fields up to 14 T. A standard lock-in technique was employed to measure the longitudinal voltage and Hall voltage in the Hall-bar geometry with an AC excitation current of 100 nA and a frequency of 13 Hz. The Hall bar channels with lengths of 800–1000 nm and widths of 140–180 nm

were chosen for the measurements. For contact wiring, no post-growth fabrication was performed. Instead, indium dots were placed and annealed at 200 °C for a few minutes on the grown InAs contact pads connected to the Hall bar channels, and the indium dots and pins on a measurement sample mount were connected via Au wires.

Further transport studies of field effect mobility, spin-orbit interaction, electron g factor, and phase coherence were conducted. E-beam lithography followed by *in situ* RF milling of the semiconductor surface before evaporating Ti/Au contacts was used to make electrical contacts to the InAs. A global Al_2O_3 dielectric was deposited before the Ti/Au top gate electrodes were evaporated. All measurements were performed at a base temperature (∼30 mK) of a cryogen-free dilution refrigerator using lock-in amplifiers at 23 Hz excitation frequency.

III. RESULTS AND DISCUSSION

In order to optimize the growth conditions for selective-area CBE of InAs on InP, the conditions for blanket growth were first studied. For conventional heteroepitaxial growth of InAs on InP, it is well known [20] that the mechanisms of initial growth and surface roughening process for InAs on InP are influenced by the surface orientation and the V/III ratio. While InAs growth on GaAs(001) tends to exhibit a distinct transition from two-dimensional (2D) layers to three-dimensional (3D) islands (Stranski-Krastanov growth mode), the InAs growth on InP is characterized as a rather gradual changing from 2D to 3D surface morphology. Under In-rich condition, the transition is suppressed and 2D InAs growth persists [21,22]. Schaffer *et al.* [23] found that InAs layers grown on GaAs(001) with In-rich condition exhibited improved structural and electrical properties. We grew InAs on InP(001) with a high V/III ratio, which led to rough 3D islands. However, a low V/III ratio (slightly In-rich condition) resulted in much improved surface morphology. The P-stabilized InP(001) surface and In-stabilized InAs(001) surface were evidenced during the growth by (2×4) and (4×2) RHEED patterns, respectively. (See Supplemental Material S2 for RHEED images [16].) The streaky (4×2) pattern was continuously observed throughout InAs growth. InAs layers grown using As-rich conditions typically show elongated spots in the [110] direction and chevron features in the [1–10] direction in the RHEED patterns. The surface morphology of 5.5-nm-thick InAs layers grown on InP(001) substrates, characterized using atomic force microscopy (AFM), are in good agreement with the previous results [24,25], which show that InAs initially forms nanometer-scale wire-like structures along the [1–10] direction with small 3D islands at the kinks. The number of kinks and size of 3D islands are found to increase with the V/III ratio, which results in a rough surface. (See Ref. [16] for AFM results.) For InP and InAsP grown on InP(111)B, Hou and Tu [26] found that a V/III incorporation ratio close to unity yielded a good surface morphology.

These optimized In-rich growth conditions for InAs blanket growth on InP(001) were then applied to selective-area CBE of InAs in-plane NWs on SiO_2-patterned InP surfaces. We found that InAs in-plane NWs formed well-defined facets on InP(001) and InP(111)B surfaces under In-rich growth conditions whereas on InP(011) surfaces well-faceted InAs NWs were seen under As-rich conditions.

A. Facets and surface energies

In Fig. 1(a), a top-view SEM image of InAs NWs grown on InP(001) substrate in the various ridge directions is shown. Starting from the [−110] direction, the NW patterns were prepared at every 15° in the counter-clockwise direction toward the [1–10] direction. This overview image reveals an excellent selectivity with no parasitic nucleation on the SiO_2 surface. Figures 1(b)–1(d) show the NWs with well-defined facets along the ridge orientations of [1–10], [110], [100], and [010], respectively. The NWs formed along the [1–10] direction possess trapezoidal cross-sections with clear {111}A-plane side facets, confirmed by structural studies using TEM/STEM. The NWs along the [110] direction, in contrast, have almost rectangular cross-sections with a small portion of {111}B-plane facets on the top edges. Although the relative portion of top-surface and side-wall facets varies with the growth conditions and ridge dimensions, the overall shapes of the NW cross-sections are in good agreement with the results reported by Krizek *et al.* [10]. The NWs grown along the ⟨100⟩ directions show the most consistent triangular cross-section with very smooth {110}-plane side facets, which was found less influenced by growth parameters.

Thermodynamics suggests that the facets of a crystal are formed such that the total surface energy is minimized. Below we calculate the ratios among the surface energies of different facets using a generic model of a trapezoidal crystal cross-section, as illustrated in Fig. 1(e). The area above the SiO_2 surface level is of interest for the calculation of the total surface energy per unit length along the NW, which is given by

$$E_{\text{total}} = L_1\gamma_1 + L_2\gamma_2 + L_3\gamma_3 + L_4\gamma_4 + L_5\gamma_5, \tag{1}$$

where L_1, L_2, L_3, L_4, and L_5 represent the lengths of facets in the cross-section and γ_1, γ_2, γ_3, γ_4 and γ_5 represent the surface energies of the facets.

For InAs NWs grown on an InP(001) substrate, the cross-sections of the NWs are symmetric ($L_1 = L_5$, $L_2 = L_4$, and $\theta_1 = \theta_2$ with θ_1 and θ_2 being angles between a plane parallel to the substrate and the facets of L_2 and L_4, respectively), and Eq. (1) becomes

$$E_{\text{total}} = 2L_1\gamma_1 + 2L_2\gamma_2 + L_3\gamma_3, \tag{2}$$

The cross-sectional area of the trapezoid as well as the width w of a NW is set to be constant:

$$\text{Area} = wL_1 + (w + L_3)(L_2 \sin\theta_1)/2 = \text{const}, \tag{3}$$

$$w = 2L_2 \cos\theta_1 + L_3 = \text{const}. \tag{4}$$

The cross-sections of the three types of NWs along [1–10], [110], and ⟨100⟩ directions on an InP(001) substrate are illustrated in Table I with details of trapezoid side lengths, angles, and corresponding facet planes, obtained from the SEM studies in Fig. 1.

Substituting L_1 and L_2 in Eq. (2) with expressions of L_3 based on Eqs. (3) and (4) leads to the total surface energy

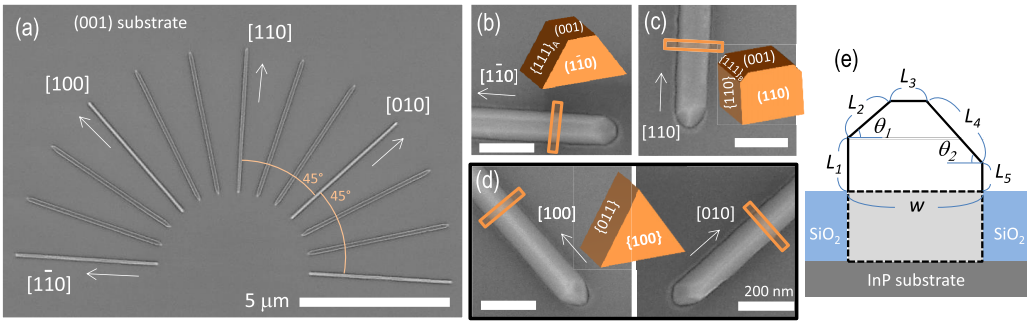

FIG. 1. InAs NWs grown on an InP(001) substrate. (a) An SEM image of InAs NWs grown on an InP(001) substrate in various ridge directions. Well-defined facets are formed in particular ridge directions: (b) [1–10], (c) [110], and (d) ⟨100⟩. Scale bars in (b)-(d): 200 nm. (e) Schematic of a generic model of a trapezoidal crystal cross-section, applied to all InAs NWs grown on InP(001), InP(111)B, and InP(011) substrates for the surface energy calculation.

E_{total} per unit length along the NW as a quadratic function of a single variable L_3. By minimizing the quadratic function, the minimum E_{total} is obtained for a condition where

$$L_3 = w\left(\frac{\gamma_2 - \gamma_3 \cos\theta_1}{\gamma_1 \sin\theta_1}\right). \tag{5}$$

Using the experimental results and applying Eq. (5), the ratio between $\gamma_{\{110\}}$, $\gamma_{\{111\}A}$, $\gamma_{\{100\}}$, and $\gamma_{\{111\}B}$ can be estimated from different conditions of the three NW ridge directions:

$$\gamma_{\{110\}} : \gamma_{\{111\}A} : \gamma_{\{100\}} : \gamma_{\{111\}B} \cong 1.0 : 1.2 : 1.4 : 1.5. \tag{6}$$

Density functional theory (DFT) has been used to calculate the surface energies γ for {110}, {100}, {111}A, and {111}B planes of InAs grown on GaAs(001) substrate as a function of As chemical potential at the surface [27]. For In-rich growth condition, the surface energies for the InAs planes are given by

$$\gamma_{\{110\}} < \gamma_{\{111\}A} < \gamma_{\{100\}} < \gamma_{\{111\}B}, \tag{7}$$

which is broadly in good agreement with the experimental results. The results from both our estimation and the DFT calculation by Moll *et al.* [27] suggest that {111}B facets are energetically unfavorable for InAs crystals grown with In-rich conditions, which explains our observation of the small sections of {111}B facets formed on the NWs along the [110] ridge direction while the top (001) facets as well as the side-wall {110} facets are clearly seen. For the crystalline shape of NWs along the ⟨100⟩ directions, the slanted {110} planes have lower surface energy than the top (001) planes, which results in triangular cross-sections.

A top-view SEM image of InAs NWs grown on an InP(111)B surface is shown in Fig. 2(a). The NWs grown along the ⟨11−2⟩ directions exhibit rectangular cross-sections with vertical {1–10} side-wall facets and flat (111)B top surfaces [Fig. 2(b)], which suggests the surface energy of the vertical {1–10} side-wall facets is the lowest for the side walls of the InAs NWs along the ⟨11−2⟩ directions, grown on InP(111)B substrates with In-rich conditions. Formation of similar vertical side-wall facets was found from recent InAs NW growths on GaAs(111)B substrates along the ⟨11−2⟩ directions [11]. We note that Friedl *et al.* [11] attributed the formation of flat (111)B top surfaces (instead of two

TABLE I. Cross-sectional shapes and facets of the InAs NWs with substrate orientations and ridge directions. Lengths (L_1–L_5) of the facets and the angles (θ_1 and θ_2) of trapezoids are defined in the generic model illustrated in Fig. 1(e).

Substrate	InP(001)			InP(111)B		InP(011)		
Channel direction	[1-10]	[110]	<100>	<1-10>	<11-2>	[100]	<111>	[0-11]
Cross section								
L	$L_1, L_5 = 0$ $L_2 = L_4$ $L_2 : L_3 \approx 1:1$	$L_1 = L_5$ $L_2 = L_4$ $L_2 : L_3 \approx 1:9$	$L_1, L_3, L_5 = 0$ $L_2 = L_4$	$L_2, L_5 = 0$ $L_3 : L_4 \approx 1:1$	$L_2, L_4 = 0$ $L_3 = w$	$L_1 = L_5$ $L_2 = L_4$ $L_2 : L_3 \approx 1:9$	$L_1 = L_5$ $L_2 = L_4$ $L_2 : L_3 \approx 1:9$	$L_2 : L_3 : L_4 \approx 1:4:4$ $L_5 = 0$
θ	$\theta_1 = 54.7°$ $\theta_2 = 54.7°$	$\theta_1 = 54.7°$ $\theta_2 = 54.7°$	$\theta_1 = 45°$ $\theta_2 = 45°$	$\theta_1 = 0°$ $\theta_2 = 54.7°$	$\theta_1 = 0°$ $\theta_2 = 0°$	$\theta_1 = 45°$ $\theta_2 = 45°$	$\theta_1 = 60°$ $\theta_2 = 60°$	$\theta_1 = 35.3°$ $\theta_2 = 35.3°$
Surface energy	$\gamma_2 = \gamma_{\{111\}A}$ $\gamma_3 = \gamma_{\{100\}}$ $\gamma_4 = \gamma_{\{111\}A}$	$\gamma_1 = \gamma_{\{110\}}$ $\gamma_2 = \gamma_{\{111\}B}$ $\gamma_3 = \gamma_{\{100\}}$ $\gamma_4 = \gamma_{\{111\}B}$ $\gamma_5 = \gamma_{\{110\}}$	$\gamma_2 = \gamma_{\{110\}}$ $\gamma_4 = \gamma_{\{110\}}$	$\gamma_1 = \gamma_{\{112\}}$ $\gamma_3 = \gamma_{\{111\}B}$ $\gamma_4 = \gamma_{\{100\}}$	$\gamma_1 = \gamma_{\{110\}}$ $\gamma_3 = \gamma_{\{111\}B}$ $\gamma_5 = \gamma_{\{110\}}$	$\gamma_1 = \gamma_{\{110\}}$ $\gamma_2 = \gamma_{\{100\}}$ $\gamma_3 = \gamma_{\{110\}}$ $\gamma_4 = \gamma_{\{100\}}$ $\gamma_5 = \gamma_{\{110\}}$	$\gamma_1 = \gamma_{\{112\}}$ $\gamma_2 = \gamma_{\{110\}}$ $\gamma_3 = \gamma_{\{110\}}$ $\gamma_4 = \gamma_{\{110\}}$ $\gamma_5 = \gamma_{\{112\}}$	$\gamma_1 = \gamma_{\{100\}}$ $\gamma_2 = \gamma_{\{111\}A}$ $\gamma_3 = \gamma_{\{110\}}$ $\gamma_4 = \gamma_{\{111\}B}$

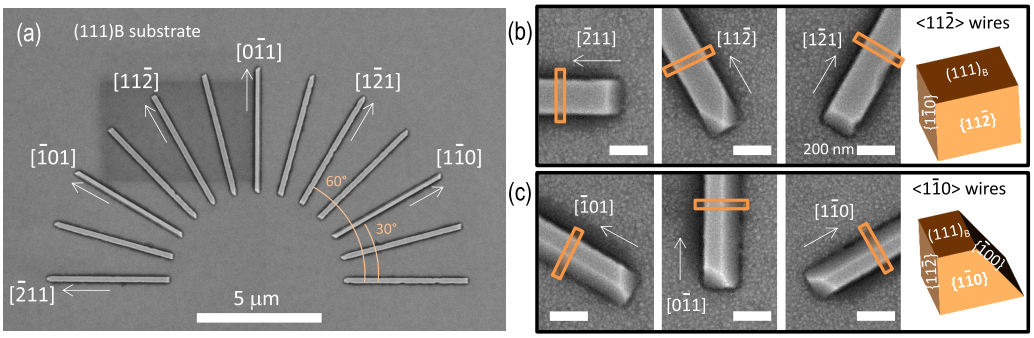

FIG. 2. InAs NWs grown on an InP(111)B substrate. (a) An SEM image of InAs NWs in various ridge directions. Well-defined facets are formed in particular ridge directions: (b) ⟨11−2⟩ and (c) ⟨1−10⟩. Scale bars in (b) and (c): 200 nm.

{113}-plane facets) of the InAs NWs grown on GaAs(111)B surfaces to the high As_4 flux used in their study. However, we also observed similar flat (111)B top surfaces with the In-rich growth conditions. For the NWs grown along the ⟨1−10⟩ ridge directions, we observed asymmetric trapezoidal cross-section consisting of slanted facets on one side, vertical side-wall facets on the other side, and flat (111)B top-surface facets as shown in Fig. 2(c). While the slanted {100} facets are some of the low-energy, low-index planes, the vertical side-wall facets appear to be high-index {11 − 2} planes.

Similarly to the surface energy estimation for InAs NWs grown on InP(001) substrates, we calculate the ratio between the surface energy $\gamma_{\{112\}}$ of {11–2} planes and other surface energies obtained previously, based on the conditions for the two types of NWs along the ⟨1−10⟩ and ⟨11−2⟩ directions grown on an InP(111)B substrate as detailed in Table I.

The total surface energy per unit length of the trapezoidal crystals grown on an InP(111)B substrate is given by

$$E_{\text{total}} = L_1\gamma_1 + L_3\gamma_3 + L_4\gamma_4 + L_5\gamma_5 \tag{8}$$

where $L_1 = L_4 \sin\theta_2 + L_5$ and $\gamma_1 = \gamma_5$. Here, the expression for area is the same as Eq. (3), and the width w is given by

$$w = L_3 + L_4 \cos\theta_2 = \text{const.} \tag{9}$$

By substituting L_4 and L_5 based on the area and the width w equations [Eqs. (3) and (9)], E_{total} is expressed as a quadratic function of a single variable L_3, and E_{total} is at a minimum when:

$$L_3 = w\left(\frac{-\gamma_3 + \gamma_4/\cos\theta_2 + \gamma_5 \tan\theta_2}{2\gamma_5 \tan\theta_2}\right). \tag{10}$$

The ratio between $\gamma_{\{112\}}$ and $\gamma_{\{100\}}$ can be estimated by applying the conditions for NWs along the ⟨1−10⟩ directions, shown in Table I. Including $\gamma_{\{112\}}$ in the previous result of Eq. (6) gives

$$\gamma_{\{110\}} : \gamma_{\{111\}A} : \gamma_{\{100\}} : \gamma_{\{111\}B} : \gamma_{\{112\}} \cong 1.0 : 1.2 : 1.4 : 1.5 : 2.4. \tag{11}$$

The surface energy of the InAs {11–2} planes has not been reported, to the best of our knowledge, while Jacobi *et al.* [28] theoretically studied the surface energy of faceted GaAs (112) planes. The results suggested that the surface energy of {112} plane is just slightly higher than those of low-index {110}, {111}A, and {111}B planes, for Ga-rich surfaces. In addition to a different material system and surface chemical potential, inclusion of strain energy possibly makes the surface energies of InAs surfaces on InP different from those of GaAs.

InAs NWs grown on InP(011) substrates form well-defined facets under As-rich growth conditions. The variation of the growth conditions from In-rich to As-rich condition could change the surface energy of each facet. Based on the DFT calculation by Moll *et al.* [27], the surface energy for InAs {111}B surface strongly depends on the As chemical potential

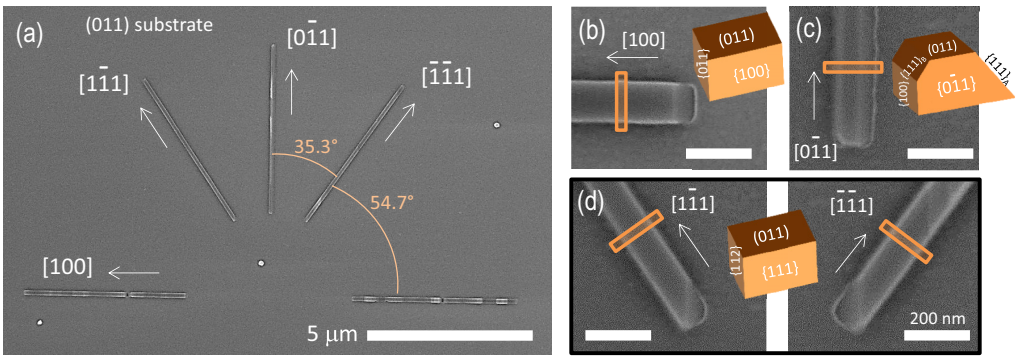

FIG. 3. InAs NWs grown on an InP(011) substrate. (a) An SEM image of the InAs NWs in various ridge directions. Well-defined facets are formed in particular ridge directions: (b) [100], (c) [0–11], and (d) ⟨111⟩. Scale bars in (b)-(d): 200 nm.

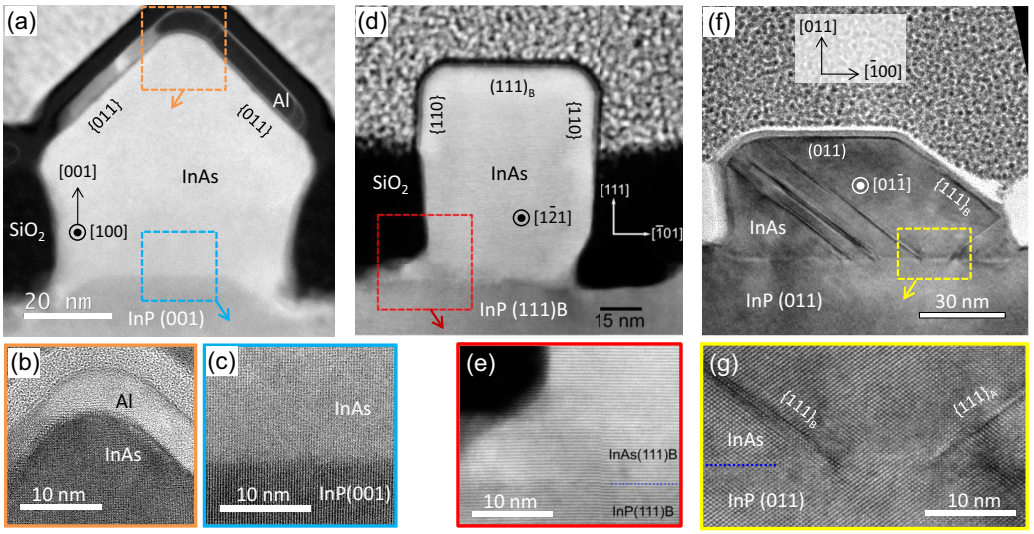

FIG. 4. STEM/TEM images of NW cross-sections perpendicular to the ridge direction. (a) A HAADF-STEM image of a NW along the [100] direction grown on an InP(001) substrate exhibits slanted {011} facets. The cross-section is viewed down the [100] zone axis (along the length of the NW). Zoom-in images reveal atomically sharp interfaces (b) between InAs and Al [orange dashed box in (a)] and (c) between InAs and InP [blue dashed box in (a)]. (d) A NW along the [1–21] direction grown on an InP(111)B substrate exhibits flat {−101} sidewalls and a $(111)_B$ top facet in its rectangular cross-section, with a slight deviation as it grows through the SiO_2 mask (region of dark contrast). (e) A higher magnification image of the interface between the InP(111)B substrate and the InAs NW shows a continuous atomic lattice without visible extended defects, which is indicative of an epitaxial growth. (f) A conventional TEM image of a NW along the [0–11] direction grown on an InP(011) substrate shows slanted {111} facets and stacking faults parallel to {111} planes. (g) A zoom-in image of the interface between the InP(011) substrate and InAs NW reveals that the stacking faults in the InAs NW originate at the interface.

at the surface, and for the As-rich growth condition:

$$\gamma_{\{111\}B} < \gamma_{\{110\}} < \gamma_{\{111\}A} < \gamma_{\{100\}}. \tag{12}$$

We estimated the surface energies of the facets on the InAs NWs grown on InP(011) substrates (Fig. 3) by the methods used for the calculation of surface energies for the InAs NWs grown on InP(001) and InP(111)B substrates under the In-rich condition determined for (001) growth. With the shape and the facet information of the NWs grown on InP(011) substrates in Table I, we obtained:

$$\gamma_{\{111\}B} : \gamma_{\{110\}} : \gamma_{\{111\}A} : \gamma_{\{112\}} : \gamma_{\{100\}} \cong 0.8 : 1.0 : 1.2 : 1.2 : 1.3, \tag{13}$$

which is qualitatively consistent with the calculation for the low-index InAs facets for As-rich conditions by Moll *et al.* [27]. We note that the result of the ratio of $\gamma_{\{110\}} : \gamma_{\{111\}A}$ from the In-rich growth condition was also applied for the As-rich growth condition in Eq. (13), as the theoretical calculation shows that $\gamma_{\{110\}}$ and $\gamma_{\{111\}A}$ values barely change as the As chemical potential is varied [27]. However the {111}B surface energy depends dramatically on the As chemical potential, suggesting that dramatic reduction in the relative surface energy of {111}B for growth on (011) surfaces [Eq. (13)] compared to (001) and (111)B surfaces [Eqs. (6) and (11)] arises from the differences in effective As chemical potential on these surfaces despite the same incident As/In flux ratio. Information on facet formation and surface energy values for lateral InAs NW grown on InP(111)B and InP(011) substrates have been relatively rare. The results reported in this work may stimulate a systematic theoretical study of lateral heterogeneous InAs NW systems.

B. Structural characterization

Detailed structural properties of InAs NWs grown on InP(001), InP(111)B, and InP(011) substrates were characterized by TEM/STEM. Cross-sections perpendicular to the ridge direction (Fig. 4) as well as cross-sections along the ridge direction (Fig. 5) were prepared from the NWs along the [100] direction grown on InP(001) substrates [Figs. 4(a)–4(c) and 5(a)–5(e)], the NWs along the [1–21] direction grown on InP(111)B substrates [Figs. 4(d), 4(e), and 5(f)–5(k)], and the NWs along the [−110] direction grown on InP(011) substrates [Figs. 4(f), 4(g), and 5(i)–5(p)]. Due to the $\sim Z^2$ dependence of image contrast in HAADF-STEM with Z being the atomic number, the SiO_2 mask appears almost black relative to the InP substrates and InAs NW structures, as shown in Figs. 4(a) and 4(d).

As suggested by top-view SEM images shown in Fig. 1(d), an InAs NW along the [100] direction grown on an InP(001) substrate has a triangular cross-section with {011}-plane side facets, confirmed by HAADF-STEM in Fig. 4(a). This InAs NW has a 7-nm-thick Al layer grown on it, and the interface between InAs and Al is atomically clean without an amorphous interfacial layer or secondary phases [Fig. 4(b)]. A higher magnification image of an interface between the InP(001) substrate and InAs(001) shows a continuous atomic lattice [Fig. 4(c)]. In Fig. 4(d), an InAs NW along the ⟨11−2⟩ direction grown on an InP(111)B substrate has rectangular cross-section with only small deviations of the {−101} side planes resulting from the mask sidewalls. After the NW grows past the mask layer, the side-walls and top facet are well defined, with small {012} corner facets present. The interface between the InP(111)B substrate and InAs(111)B NW shows

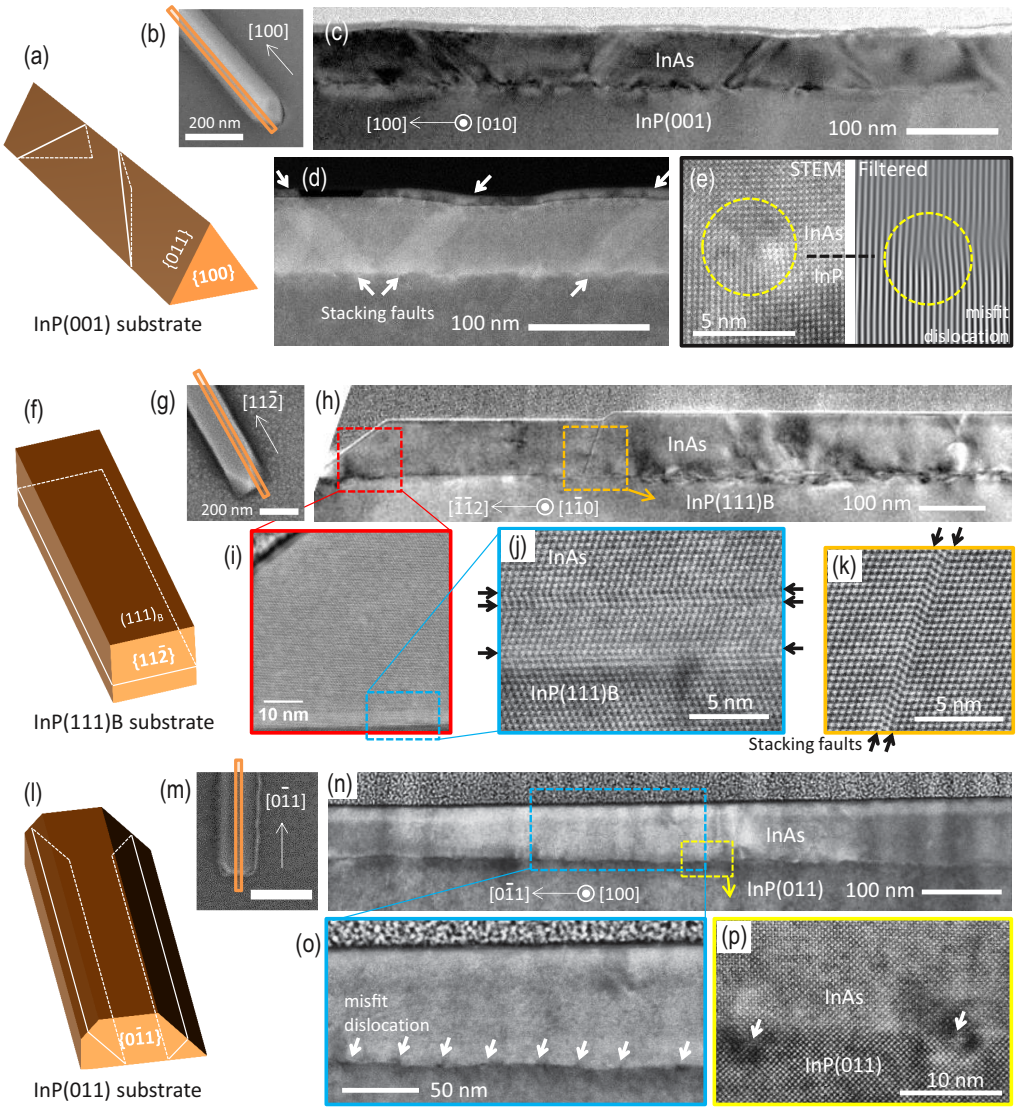

FIG. 5. STEM/TEM images of NW cross-sections along the ridge direction. (a) A schematic and (b) an SEM image of a NW along the [100] direction grown on an InP(001) substrate. White lines in the schematic represent {111} planes in the NW, and the orange rectangle in the SEM image represents the position of the prepared cross-section. A conventional TEM image in (c) and an HAADF-STEM image in (d) reveal the inclined {111} stacking fault planes across the NW, indicated by white arrows in (d). (e) A misfit dislocation at the interface between InP and InAs is seen in an HAADF-STEM image and a Fourier filtered image. (f) A schematic and (g) an SEM image of a NW along [11–2] direction grown on an InP(111)B substrate. A conventional TEM image of the cross-section of the NW. Zoom-in images of the stacking faults [(i) and (j)] near the interface between the InP(111)B substrate and InAs NW and (k) a grain boundary. Black arrows represent the stacking fault planes. (l) A schematic and (m) an SEM image of a NW along [0–11] direction grown on an InP(011) substrate. (n) A HAADF-STEM image of the cross-section of the NW. [(o) and (p)] Zoom-in images show misfit dislocations at the interface between the InP(011) substrate and InAs NW.

a well-defined atomic lattice [Fig. 4(e)]. Figures 4(f) and 4(g) show conventional TEM images of an InAs NW along the [0–11] direction grown on an InP(011) substrate. In the cross-section of the NW, stacking faults parallel to the {111} side-wall facets are clearly seen. In cubic III-V compound semiconductors, the low stacking fault energy results in the formation of the stacking faults on {111} planes [29]. Charge transport properties of the InAs NWs may be affected by the defects and the correlated strain fields, and thus studies of defects and disorder in the SAE NWs could be important for potential electronic device applications.

We further investigate the defects formed along the ridge direction of the InAs NWs grown on InP(001), InP(111)B, and InP(011) substrates. InAs NWs grown on InP(001) substrates have inclined {111} planes across the NWs as schematically illustrated in Fig. 5(a). Conventional TEM and HAADF-STEM of the cross-section along the [100] ridge direction confirms that the stacking faults form on the inclined {111} planes [Figs. 5(c) and 5(d)]. The white arrows, shown in Fig. 5(d), indicate the stacking fault planes. The stacking fault planes look broad because {111} planes are inclined from the [010] zone axis and the TEM lamella has a

finite thickness (∼50 nm). We also observed misfit dislocations caused by the 3.3% lattice mismatch between InP and InAs. A Fourier-filtered image from an HAADF-STEM image clearly shows a misfit dislocation at the interface [Fig. 5(e)].

For the NWs grown on InP(111)B substrates, the stacking faults form on the {111} planes that are parallel to the growth plane as schematically illustrated in Fig. 5(f). From a cross-section of an InAs NW along the [11–2] ridge direction, stacking faults parallel to the (111)B substrate plane as well as across the NW ridge direction were seen in a conventional TEM image in Fig. 5(h). HAADF-STEM images reveal multiple stacking faults in InAs near the interface between the InP substrate and the InAs layer [Figs. 5(i) and 5(j)]. The stacking faults across the NW ridge direction [Fig. 5(k)] are also formed on the {111} planes near the grain boundaries.

In the InAs NWs along the [0–11] direction grown on InP(011) substrates, stacking faults on the {111} planes are parallel to the ridge direction and the inclined side-wall facets [Fig. 5(l)]. The stacking faults may not be seen depending on where the NW is cut along the ridge direction, as in the HAADF-STEM image in Fig. 5(n), whereas multiple stacking faults were observed in a cross-section perpendicular to the ridge direction as shown in Fig. 4(f). STEM images of the interface between InP(011) and InAs(011) along the ridge direction [Figs. 5(o) and 5(p)] reveal misfit dislocations with a density of $3 \times 10^5\,\mathrm{cm}^{-1}$, indicating that the InAs layer grown under the As-rich condition is mostly relaxed on the InP(011) substrate. (The misfit dislocation density of fully relaxed InAs on InP is expected to be $5 \times 10^5\,\mathrm{cm}^{-1}$.)

C. Electrical transport properties

As evidenced in the studies of the surface energy and structural characterization, NW facet formation shows a strong dependence on substrate orientation and ridge direction. An important follow-up question will be if the substrate orientation and the ridge direction affect the transport properties of NWs. To answer this question and thus to optimize the configuration of NW networks, we prepared InAs NW Hall bar structures on SiO_2-patterned InP(001), InP(111)B, and InP(011) substrates as shown in Fig. 6(a). The Hall bars were made along the [1–10], [110], and ⟨100⟩ directions on an InP(001) substrate, the ⟨1−10⟩ and ⟨11−2⟩ directions on an InP(111)B substrate, and the [100], [0–11], and ⟨111⟩ directions on an InP(011) substrate. The InAs Hall bar channels are in the diffusive transport regime where the channel length (L = 800–1000 nm) is longer than the elastic mean-free path (20–100 nm) with the channel widths of 130–180 nm. Figures 6(b)–6(i) show that the resulting magnetoresistance (longitudinal channel resistance as a function of perpendicular magnetic field) and Hall resistance vary with substrate orientations and ridge directions. We note that the Hall resistance linearly depends on the magnetic field, and the fluctuations in the Hall resistance are from a mix of longitudinal resistance and Hall resistance. The magnetoresistance fluctuations, observed in all channels on InP(001), InP(111)B, InP(011) substrates, are reproducible and identical in both positive and negative magnetic fields, so they can be referred to as universal conductance fluctuations [30]. Weak localization (WL) correction to magnetoconductance has been reported in self-assembled and etch-defined InAs NWs in the case where the phase coherence length l_ϕ is smaller than the spin-orbit interaction length l_{SO} [31–33]. However, we do not attribute the negative magnetoresistance to WL because of the large amplitude of the conductance fluctuations in the InAs Hall bar channels, measured at 2 K. In the following section, weak antilocalization (WAL) correction to magnetoconductance will be further discussed using an InAs NW with a top gate.

Carrier density n and charge mobility μ were calculated based on the results of the longitudinal resistance and Hall measurements. In addition, the electron mean-free path l_e was calculated by $l_e = e\hbar\mu k_F$, where e, $\hbar$, and k_F are electron charge, reduced Planck constant, and the Fermi wave vector, respectively. Table II summarizes the carrier density, mobility, and mean-free path as a function of substrate orientation and NW ridge direction. Overall ranges of carrier density, mobility, and mean-free path are within $0.9–2.1 \times 10^{17}\,\mathrm{cm}^{-3}$, $1000–5000\,\mathrm{cm}^2\,\mathrm{V}^{-2}\,\mathrm{s}^{-1}$, and 20–100 nm, respectively. Due to differences in carrier density, direct comparison of charge mobility in various NWs is not viable. Gate-voltage tuning of the carrier density will be necessary for the comparison. The values of the obtained mobilities are comparable to earlier measurements on InAs NWs. We speculate that by changing the buffer layer material or thickness the mobility can be further increased.

D. Phase-coherent quantum transport

Here, we further perform electrical transport characterization in SAE InAs NWs grown on InP(001) substrates. In order to obtain field effect mobility μ_{fe}, conductance of an InAs NW structure along the [1–10] direction with the width $w \sim 140$ nm was measured as a function of gate voltage V_G at ∼30 mK. In the case of diffusive transport, the conductance can be written as $g(V_g) = \frac{\mu_{fe}C}{L^2}(V_g - V_{\mathrm{th}})$, where C is the gate capacitance, L is the gated segment length, and V_{th} is the threshold voltage. By defining the transconductance $g_t = \frac{\partial g}{\partial V_g}$, for known C and L, the field effect mobility can be determined. A linear fit to the steepest part of the pinch off curve [red line in Fig. 7(a)] yields the peak transconductance. From $L \sim 3.4\,\mu$m and numerically simulated $C \sim 1.7$ fF, we estimate a field effect mobility of $\sim 2000\,\mathrm{cm}^2/\mathrm{V\,s}$, which is within the range of the charge mobility obtained by the Hall measurements.

Next, we focus on characterizing spin-orbit interaction in the SAE InAs by magnetotransport. The device shown in the Fig. 7(a) inset was measured in an out-of-plane magnetic field B. The differential magnetoconductance $\langle \Delta g \rangle$ is averaged over a gate voltage window of 80 mV to suppress universal conductance fluctuations and offset to be zero at $B = 0$. Figure 7(b) plots $\langle \Delta g \rangle(B)$ at $V_g = 0$ V (purple) and $V_g = -1.2$ V (green). The WAL peak at $B = 0$ is clearly visible in both traces, indicating strong spin-orbit coupling over the whole gate-voltage range. To get a measure for the phase coherence length l_ϕ and the spin-orbit length l_{SO}, one can model the WAL correction to conductance. Different models can lead to different length scales, but in order to compare to literature

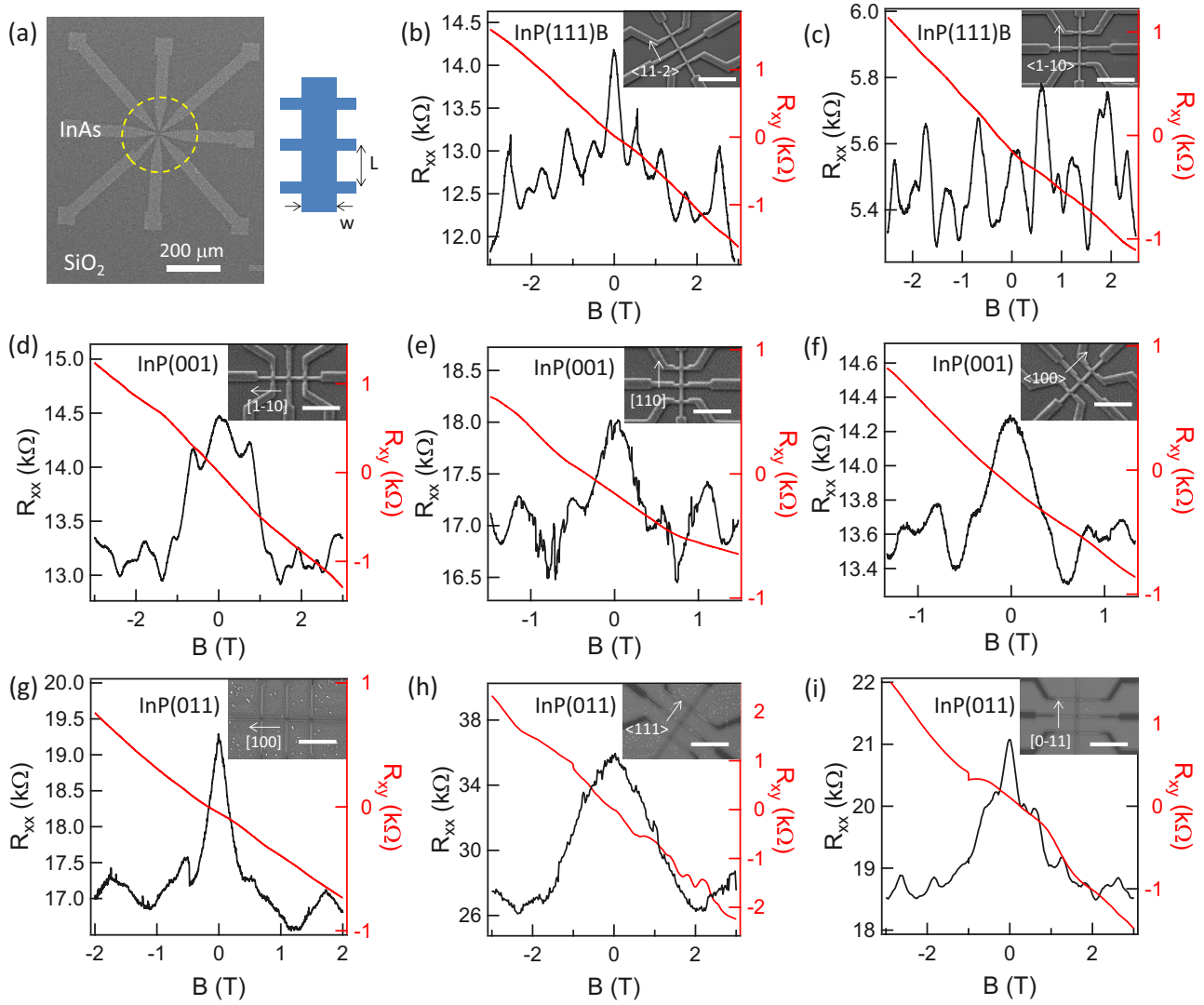

FIG. 6. Hall measurements using a Hall bar geometry. (a) A low-magnification SEM image shows contact pads extended from a Hall bar, in the yellow dashed circle, illustrated as a schematic. Longitudinal resistance (black curves) and Hall resistance (red curves) were measured using Hall bar channels with various substrate orientations and channel directions: (b) along ⟨11−2⟩ direction and (c) ⟨1−10⟩ direction grown on an InP(111)B substrate, (d) along [1–10] direction, (e) [110] direction, and (f) ⟨100⟩ direction grown on an InP(001) substrate, and (g) along [100] direction, (h) ⟨111⟩ direction, and (i) [0–11] direction grown on an InP(011) substrate. (Insets) SEM images of measured Hall bars (scale bar: 2 μm). All measurements were carried out at 2 K.

TABLE II. Transport properties of the InAs NWs of various substrate orientations and channel directions, obtained at 2 K. n, μ, and l_e represent the carrier density, charge mobility, and mean-free path, respectively.

Substrate	Channel directions	Channel width w	Channel length L	n (10^{17} cm^{-3})	μ (cm^2 V^{-2} s^{-1})	l_e (nm)
InP(001)	[110]	180 nm	800 nm	1.32	1170	22
InP(001)	[1–10]	170 nm	800 nm	1.43	1420	28
InP(001)	⟨100⟩	160 nm	800 nm	0.89	2450	38
InP(111)B	⟨11−2⟩	140 nm	800 nm	1.14	2430	43
InP(111)B	⟨1−10⟩	140 nm	800 nm	1.35	4760	91
InP(011)	[100]	130 nm	1000 nm	2.07	1040	22
InP(011)	⟨111⟩	130 nm	1000 nm	1.04	1520	23
InP(011)	[0–11]	130 nm	1000 nm	1.55	1840	34

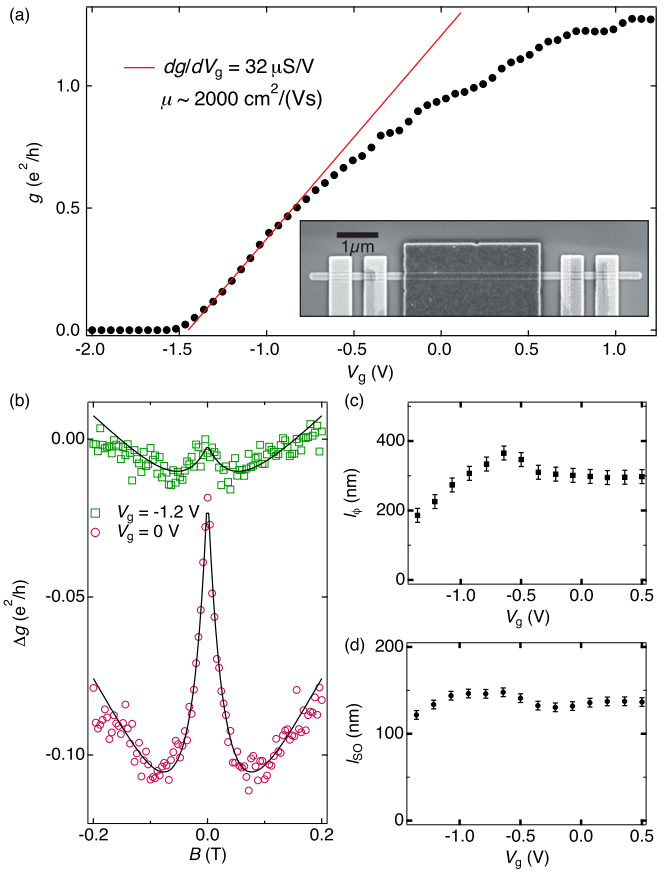

FIG. 7. Transport characterization of field effect mobility and WAL. (a) Differential conductance of a selectively grown InAs NW as a function of gate voltage V_g. The solid red line is a linear fit to extract the peak in transconductance g_t. The inset shows an SEM image of the field effect mobility device. (b) Magnetoconductance Δg, offset to zero at zero field for two different gate voltages. The two curves are vertically offset. The WAL peaks are fitted with functions described in the main text (black curves). [(c) and (d)] Extracted phase coherence length l_ϕ (c) and spin-orbit length l_{SO} (d) from WAL fits as a function of V_g.

values we follow the commonly used model which is valid in the diffusive limit ($l_{el} \ll w$). The magnetoconductance is expressed as

$$\Delta g(B) \propto \frac{3}{2}\left(\frac{1}{l_\phi^2}+\frac{1}{3l_{SO}^2}+\frac{1}{D_{\tau_B}}\right)^{-\frac{1}{2}}-\frac{1}{2}\left(\frac{1}{l_\phi^2}+\frac{1}{D_{\tau_B}}\right)^{-\frac{1}{2}}, \tag{14}$$

where the magnetic dephasing time is given by $\tau_B = \frac{Cl_m^4}{w^2 D}$ with D being the diffusion constant and $l_m = \sqrt{\frac{h}{eB}}$ being the magnetic length, which is on the order of the NW diameter for the fitting range ~0.18 T. The prefactor C is geometry and system dependent. To allow for a comparison to previous work on InAs NWs, we use $C = 3$. The black curves in Fig. 7(b) show the fits of Eq. (14) to the data using a fixed w. The extracted l_{SO} and l_ϕ of ~140 nm and ~300 nm, respectively, are in agreement with previous experiments on InAs NWs [31–33]. As a function of gate voltage, both length scales l_{SO} and l_ϕ decrease at negative gate voltage [Figs. 7(c) and 7(d)]. This reduction has been attributed to a suppression of spin-orbit coupling in the NWs and thus the disappearance of the WAL peak [32,33], which is consistent with the data in Fig. 7(b).

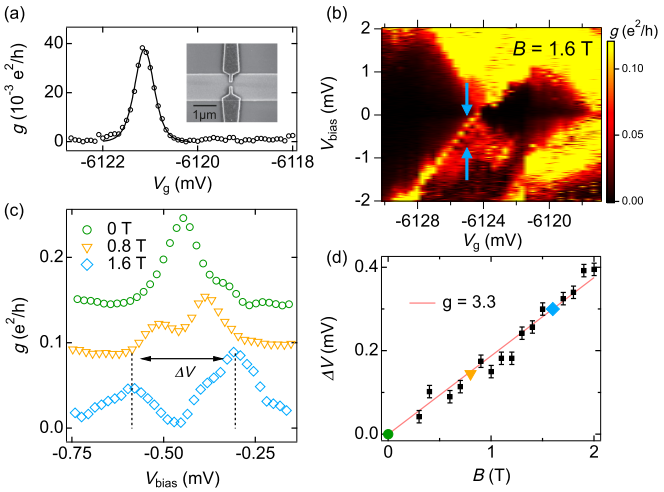

FIG. 8. Measurement of the electron g factor. (a) Coulomb peak close to pinch off in the split-gate geometry. Inset: an SEM image of the split-gate device. (b) The differential conductance g is plotted as a function of V_{bias} and V_g in the Coulomb blockade regime at an in-plane field $B = 1.6$ T. (c) Cuts along V_{bias} at a fixed V_g for different magnetic fields. The curves are shifted horizontally and vertically for clarity. (d) The extracted ΔV for different in-plane fields with a linear fit to the data (red line).

We now present measurements of the electron g factor in the InAs structures along the [1–10] direction. The inset of Fig 8(a) shows an SEM image of a device that was fabricated on a wide InAs slab and has two split-gate electrodes operating symmetrically with a gate voltage V_g. When pinching off the two gates, sharp peaks in conductance were observed [Fig. 8(a)], which we interpret as the Coulomb blockade due to some accidentally formed quantum dot. We use bias spectroscopy to quantify the electron g factor [34]. In Fig. 8(b), the differential conductance is plotted as a function of V_g and the bias voltage V_{bias} in an in-plane magnetic field $B = 1.6$ T, exhibiting typical Coulomb diamonds. Additional lines appear outside of the blockaded region at larger V_{bias}, indicating exited states. A cut at a constant V_g (blue arrows) shows two distinct peaks as seen in Fig. 8(c). At a lower magnetic field, $B = 0.8$ T (orange), the peak splitting reduces, and at $B = 0$ T (green) there is only one single peak visible. We interpret the peak splitting ΔV as the Zeeman splitting of the quantum dot level with $\Delta V = g\mu_B B/e$, where μ_B is the Bohr magneton. Figure 8(d) plots ΔV for different fields. We find that for $B < 0.4$ T and $\Delta V < 80\,\mu$V it is difficult to extract a splitting. We suspect that the quantum dot level is tunnel broadened, and thus the line width is not temperature limited. A linear fit to $\Delta V(B)$ [red line in Fig. 8(d)] yields an electron g factor of 3.3. This value is consistent with a wide spread in g factors measured in InAs quantum dots [35].

Finally, we investigate the phase-coherent transport based on the Aharonov-Bohm (AB) effect in an SAE InAs loop structure. Conductance through the loop threaded with flux Φ, given for various temperatures, was measured. The obtained

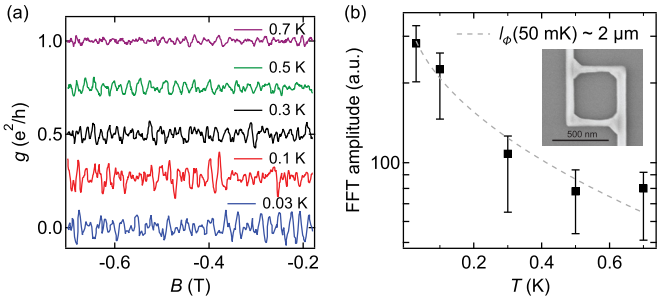

FIG. 9. Measurement of the electron phase coherence length l_ϕ in an AB geometry. (a) Magnetoconductance with subtracted background as a function of out-of-plane magnetic field B for different temperatures. Curves are vertically offset for clarity. (b) Integrated FFT of the oscillations plotted as a function of temperature. The fit (dashed grey line) corresponds to the amplitude decay within the diffusive regime with $l_\phi \sim 2\,\mu$m at 50 mK. (Inset) An SEM image of a grown AB loop.

oscillations have the period $h/e = \Phi \cdot S$, consistent with the measured area S of the AB loop. Figure 9(a) shows the measured conductance at various temperatures between 30 mK and 700 mK. Slowly-varying background was subtracted from each curve. Curves are offset for clarity. Each curve was then Fourier-transformed, and the fast Fourier transform (FFT) amplitude in Fig. 9(b) denotes the value of the integrated first-harmonic peak. The integration limits are given by the inner and outer ring circumferences, as measured from an SEM image [Fig. 9(b) inset]. Error bars stem from the uncertainty in measuring AB loop dimensions. The decay of the AB FFT amplitude, shown in Fig. 9(b), was then fitted to $a\exp(-l/l_\phi(T))$, where l is the length of one arm of the loop, l_ϕ is the electron coherence length, and a is a constant. We assume $l_\phi \propto T^{-1/2}$, the case for a diffusive transport. A curve fitting from the dependence assuming a ballistic transport $l_\phi \propto T^{-1}$ was attempted but it did not fit as well. The phase coherence length l_ϕ is found to be 2 μm or roughly the ring circumference at 50 mK. The resulting values of the phase coherence length from the AB effect differ from the phase coherence length from WAL, which is likely due to the fact that the dephasing process governing the two effects is different [36].

IV. CONCLUSIONS

InAs in-plane NWs were selectively grown on SiO_2-patterned InP(001), InP(111)B, and InP(011) substrates by CBE with excellent surface selectivity. At the substrate temperature of ~520 °C, slightly In-rich growth conditions yielded InAs NWs with smooth surface morphology on InP(001) and InP(111)B surfaces whereas As-rich growth conditions resulted in InAs NWs with well-defined facets on an InP(011) surface. Faceting of the InAs NWs largely depends on the surface orientation and the ridge direction of the InAs NWs. On (001) surfaces, the NWs that formed along the [1–10] direction possess trapezoidal cross-sections with clear {111}A-plane side facets while the NWs that formed along the [110] direction have almost rectangular cross-sections with a small portion of {111}B-plane facets on the top edges. The NWs grown between those two directions, along the [010] direction, have triangular cross-sections with smooth {110}-plane side facets. On (111)B surfaces, the NWs grown in the ⟨1−10⟩ direction show asymmetric trapezoidal cross-sections with slanted {100} and vertical {11–2} side-wall facets and flat (111)B top surfaces, whereas the NWs grown in the ⟨11−2⟩ direction exhibit rather rectangular cross-sections with vertical {1–10} facets and flat (111)B top surfaces. On (011) surfaces, rectangular cross-sections are seen in the NWs grown in the [100] and ⟨111⟩ directions while asymmetric trapezoidal cross-sections with slanted {111} side-wall facets and flat (011) top surfaces are observed in the NWs grown in the [0–11] direction.

The ratios of the surface energies of the observed facet surfaces were estimated based on the structural characterization. The results as ratios are qualitatively consistent with theoretical predictions for both In-rich and As-rich growth conditions. STEM/TEM of cross-sections perpendicular to ridge directions and cross-sections along ridge directions further reveals the atomic structures of interfaces between the InAs NWs and InP(001), InP(111)B, and InP(011) substrates, as well as defects in the NWs. A continuous atomic lattice with misfit dislocations was observed at the interface. These dislocations were due to the lattice mismatch between InAs and InP. Multiple stacking faults of inclined {111} planes were observed along the ridge directions in the InAs NWs grown on an InP(001) substrate whereas stacking fault planes were found to be parallel to the substrate in the NWs grown on an InP(111)B substrate. In the NWs along [0–11] direction grown on an InP(011) substrate, stacking faults are parallel to both the ridge direction and the inclined {111} side-wall facets.

Electrical transport properties were characterized using selectively grown Hall bar channels on various ridge directions grown on InP(001), InP(111)B, and InP(011) substrates. Obtained carrier density and mobility of the InAs channels, measured at 2 K, are in the range of 0.9–2.1 × 10^{17} cm^{-2} and 1000–5000 $cm^2\,V^{-2}\,s^{-1}$, respectively. The mobility of the InAs NWs grown on InP(001) substrates was confirmed by field effect mobility. From WAL correction to the conductance using the field effect mobility device, spin-orbit length l_{SO} and phase coherence length l_ϕ was estimated to be ~140 and ~300 nm, respectively. The WAL is suppressed by applying negative gate-voltage tuning, which corresponds to decreases in l_{SO} and l_ϕ. The electron g factor in an InAs slab along the [1–10] direction with two split-gate electrodes was estimated to be 3.3 based on the Zeeman splitting of a quantum dot level. Phase-coherent transport in an AB loop geometry revealed the phase coherence length l_ϕ to be ~2 μm at 50 mK, which suggests that the conductance-interferometry-based measurement schemes of braiding [37,38] could be viable in these SAE InAs systems.

ACKNOWLEDGMENTS

This work was supported by Microsoft Research Station Q and the Danish National Research Foundation. Patterned substrates were prepared in UCSB Nano-fabrication Facility, and most of the structural characterization studies were performed at the UCSB MRL Shared Experimental Facilities

(NSF DMR-1720256), a member of the NSF-funded Materials Research Facility Network. The patterning development was supported by NSF (NSF ECCS-1640030). C.M.M. acknowledges support from the Villum Foundation. Solliance and the Dutch province of Noord-Brabant are acknowledged for funding the probe-corrected STEM facility.

[1] R. M. Lutchyn, J. D. Sau, and S. Das Sarma, Phys. Rev. Lett. **105**, 077001 (2010).
[2] Y. Oreg, G. Refael, and F. von Oppen, Phys. Rev. Lett. **105**, 177002 (2010).
[3] V. Mourik, K. Zuo, S. M. Frolov, S. R. Plissard, E. P. A. M. Bakkers, and L. P. Kouwenhoven, Science **336**, 1003 (2012).
[4] A. Das, Y. Ronen, Y. Most, Y. Oreg, M. Heiblum, and H. Shtrikman, Nat. Phys. **8**, 887 (2012).
[5] M. T. Deng, C. L. Yu, G. Y. Huang, M. Larsson, P. Caroff, and H. Q. Xu, Nano Lett. **12**, 6414 (2012).
[6] H. O. H. Churchill, V. Fatemi, K. Grove-Rasmussen, M. T. Deng, P. Caroff, H. Q. Xu, and C. M. Marcus, Phys. Rev. B **87**, 241401(R) (2013).
[7] H. Schmid, M. Borg, K. Moselund, L. Gignac, C. M. Breslin, J. Bruley, D. Cutaia, and H. Riel, Appl. Phys. Lett. **106**, 233101 (2015).
[8] M. Fahed, L. Desplanque, D. Troadec, G. Patriarche, and X. Wallart, Nanotechnology **27**, 505301 (2016).
[9] S. Vaitiekėnas, A. M. Whiticar, M.-T. Deng, F. Krizek, J. E. Sestoft, C. J. Palmstrøm, S. Marti-Sanchez, J. Arbiol, P. Krogstrup, L. Casparis, and C. M. Marcus, Phys. Rev. Lett. **121**, 147701 (2018).
[10] F. Krizek, J. E. Sestoft, P. Aseev, S. Marti-Sanchez, S. Vaitiekėnas, L. Casparis, S. A. Khan, Y. Liu, T. Stankevič, A. M. Whiticar, A. Fursina, F. Boekhout, R. Koops, E. Uccelli, L. P. Kouwenhoven, C. M. Marcus, J. Arbiol, and P. Krogstrup, Phys. Rev. Mater. **2**, 093401 (2018).
[11] M. Friedl, K. Cerveny, P. Weigele, G. Tütüncüoglu, S. Martí-Sánchez, C. Huang, T. Patlatiuk, H. Potts, Z. Sun, M. O. Hill, L. Güniat, W. Kim, M. Zamani, V. G. Dubrovskii, J. Arbiol, L. J. Lauhon, D. M. Zumbühl, and A. Fontcuberta i Morral, Nano Lett. **18**, 2666 (2018).
[12] L. Desplanque, A. Bucamp, D. Troadec, G. Patriarche, and X. Wallart, Nanotechnology **29**, 305705 (2018).
[13] P. Aseev, A. Fursina, F. Boekhout, F. Krizek, J. E. Sestoft, F. Borsoi, S. Heedt, G. Wang, L. Binci, S. Martí-Sánchez, T. Swoboda, R. Koops, E. Uccelli, J. Arbiol, P. Krogstrup, L. P. Kouwenhoven, and P. Caroff, Nano Lett. **19**, 218 (2019).
[14] J. S. Foord, G. J. Davies, and W. T. Tsang, *Chemical Beam Epitaxy and Related Techniques* (Wiley, Chichester, 1997).
[15] G. J. Davies, W. J. Duncan, P. J. Skevington, C. L. French, and J. S. Foord, Mater. Sci. Eng. B **9**, 93 (1991).
[16] See Supplemental Material at http://link.aps.org/supplemental/10.1103/PhysRevMaterials.3.084606 for S1, substrate preparation procedures; S2, reflection high-energy electron diffraction of InP and InAs surfaces; and S3, atomic force microscopy of thick InAs layers.
[17] V. J. Mifsud, P. W. Sullivan, and D. Williams, J. Cryst. Growth **105**, 289 (1990).
[18] S. Gazibegovic, D. Car, H. Zhang, S. C. Balk, J. A. Logan, M. W. A. De Moor, M. C. Cassidy, R. Schmits, D. Xu, G. Wang, P. Krogstrup, R. L. M. Op Het Veld, K. Zuo, Y. Vos, J. Shen, D. Bouman, B. Shojaei, D. Pennachio, J. S. Lee, P. J. Van Veldhoven, S. Koelling, M. A. Verheijen, L. P. Kouwenhoven, C. J. Palmstrøm, and E. P. A. M. Bakkers, Nature **548**, 434 (2017).
[19] H. Zhang, C. X. Liu, S. Gazibegovic, D. Xu, J. A. Logan, G. Wang, N. Van Loo, J. D. S. Bommer, M. W. A. De Moor, D. Car, R. L. M. Op Het Veld, P. J. Van Veldhoven, S. Koelling, M. A. Verheijen, M. Pendharkar, D. J. Pennachio, B. Shojaei, J. S. Lee, C. J. Palmstrøm, E. P. A. M. Bakkers, S. Das Sarma, and L. P. Kouwenhoven, Nature **556**, 74 (2018).
[20] P. Bhattacharya, R. Fornari, and H. Kamimura, *Comprehensive Semiconductor Science and Technology* (Elsevier Science, Amsterdam, 2011).
[21] E. Tournié and K. H. Ploog, Appl. Phys. Lett. **62**, 858 (1993).
[22] L. Goldstein, F. Glas, J. Y. Marzin, M. N. Charasse, and G. Le Roux, Appl. Phys. Lett. **47**, 1099 (1985).
[23] W. J. Schaffer, M. D. Lind, S. P. Kowalczyk, and R. W. Grant, J. Vac. Sci. Technol. B Microelectron. Nanom. Struct. **1**, 688 (1983).
[24] H. J. Parry, M. J. Ashwin, J. H. Neave, and T. S. Jones, J. Cryst. Growth **278**, 131 (2005).
[25] C. Walther, W. Hoerstel, H. Niehus, J. Erxmeyer, and W. T. Masselink, J. Cryst. Growth **209**, 572 (2000).
[26] H. Q. Hou and C. W. Tu, J. Cryst. Growth **127**, 199 (1993).
[27] N. Moll, M. Scheffler, and E. Pehlke, Phys. Rev. B **58**, 4566 (1998).
[28] K. Jacobi, J. Platen, C. Setzer, J. Maárquez, L. Geelhaar, C. Meyne, W. Richter, A. Kley, P. Ruggerone, and M. Scheffler, Surf. Sci. **439**, 59 (1999).
[29] H. Gottschalk, G. Patzer, and H. Alexander, Phys. Stat. Sol. **45**, 207 (1978).
[30] P. A. Lee and A. D. Stone, Phys. Rev. Lett. **55**, 1622 (1985).
[31] A. E. Hansen, M. T. Björk, C. Fasth, C. Thelander, and L. Samuelson, Phys. Rev. B **71**, 205328 (2005).
[32] S. Dhara, H. S. Solanki, V. Singh, A. Narayanan, P. Chaudhari, M. Gokhale, A. Bhattacharya, and M. M. Deshmukh, Phys. Rev. B **79**, 121311(R) (2009).
[33] P. Roulleau, T. Choi, S. Riedi, T. Heinzel, I. Shorubalko, T. Ihn, and K. Ensslin, Phys. Rev. B **81**, 155449 (2010).
[34] R. Hanson, B. Witkamp, L. M. K. Vandersypen, L. H. Willems van Beveren, J. M. Elzerman, and L. P. Kouwenhoven, Phys. Rev. Lett. **91**, 196802 (2003).
[35] S. Csonka, L. Hofstetter, F. Freitag, S. Oberholzer, C. Schönenberger, T. S. Jespersen, M. Aagesen, and J. Nygård, Nano Lett. **8**, 3932 (2008).
[36] T. Ludwig and A. D. Mirlin, Phys. Rev. B **69**, 193306 (2004).
[37] S. Vijay and L. Fu, Phys. Rev. B **94**, 235446 (2016).
[38] T. Karzig, C. Knapp, R. M. Lutchyn, P. Bonderson, M. B. Hastings, C. Nayak, J. Alicea, K. Flensberg, S. Plugge, Y. Oreg, C. M. Marcus, and M. H. Freedman, Phys. Rev. B **95**, 235305 (2017).